# Discover Nano

**Research**

# Assemble of porous heterostructure thin film through CuS passivation for efficient electron transport in dye-sensitized solar cells

Mojeed A. Agoro[1,2] · Edson L. Meyer[1] · Olufemi I. Olayiwola[3]

## Abstract

Three different modified solar cells have been passivated with copper sulfide (CuS) on a $TiO_2$ electrode and manganese sulfide (γ-MnS) hexagonal as photon absorbers. The MnS were prepared using (a-c) *bis*(*N*-Piperl-*N*-*p*-anisildithiocarbamato)Manganese(II) Complexes Mn[*N*-Piper-*N*-*p*-Anisdtc] as (MnS_1), *N*-*p*-anisidinyldithiocarbamato Mn[*N*-*p*-anisdtc] as (MnS_2) and *N*-piperidinyldithiocarbamato Mn[*N*-piperdtc] as (MnS_3). The corresponding passivated films were denoted as CM-1, CM-2, and CM-3. The influence of passivation on the structural, optical, morphological, and photochemical properties of the prepared devices has been investigated. Raman spectra show that the combination of this heterostructure is triggered by the variation in particle size and surface effect, thus resulting in good electronic conductivity. The narrow band gaps could be attributed to good interaction between the passivative materials on the $TiO_2$ surface. CM-2 cells, stability studies show that the cell is polarized and current flows due to electron migration across the electrolyte and interfaces at this steady state. The cyclic voltammetry (CV) curve for the CM-3 with the highest current density promotes the electrocatalytic activity of the assembled solar cell. The catalytic reactions are further confirmed by the interfacial electron lifetimes in the Bode plots and the impedance spectra. The current–voltage (*J–V*) analysis suggests that the electrons in the conduction band of $TiO_2$/CuS recombine with the semiconductor quantum dots (QDs) and the iodolyte HI-30 electrolyte, resulting in 5.20–6.85% photo-conversions.

## 1 Introductions

Energy demand is directly linked to the global economy's rapid development in the twenty-first century for both developed and underdeveloped countries. Solar cells have continued to increase since the past three decades due to their considerable achievements, regarding them as one of the main sources of future power [1–3]. Because of their high stability and absorption, conversional dye-sensitized solar cells (DSSCs) efficiently convert sunlight into electricity. The greater efficiency of more than 11% by photoelectric conversion efficiency (PCE) has reached greater conduction for the rigid planar substrate-based DSSCs [4, 5]. The introduction of semiconductor quantum dots (QDs) as a substitution in sensitizers for organic dyes shows the distinctive benefits of matching the energy levels of the material electron donor and acceptor, quantum size effect, large absorption coefficient, and multi-exciton effect [6, 7]. Numerous QDs have been reported for quantum dot-sensitized solar cells (QDSSCs) [8–11]. Co-sensitization of these semiconductor QDs

✉ Mojeed A. Agoro, magoro@ufh.ac.za | [1]Fort Hare Institute of Technology, University of Fort Hare, Private Bag X1314, Alice 5700, Eastern Cape, South Africa. [2]Department of Chemistry, University of Fort Hare, Private Bag X1314, Alice 5700, Eastern Cape, South Africa. [3]Institute for Safe Autonomy, University of York, York YO10 5FT, UK.

Discover

with TiO$_2$ has also shown a good effect on the deposition of QDs, forming a classical cascade structure, as reported by Lee and Lo [12]. Doping of Mn$^{2+}$ into CDS QDs by the Santra and Kamat study [13] enhances the PCE of the QDSCs; this considerable increase of approximately 9%, which is still below the 15% highest efficiency obtained by DSSCs [14–17]. Easy photoelectrons are obtained through transmission in the presence of surface defects on the nanoparticle surface, which increases the photoelectron recombination probability. The introduction of co-sensitization of transition metal sulfides such as copper sulfide (CuS) and manganese sulfide (MnS) is a promising material to reduce photoelectron recombination possibility and modify the QD intrinsic properties [18].

CuS is widely used due to its optical, structural, and electrical properties in various applications such as energy conversion and storage [19]. CuS appears in several phases with different stoichiometries, from covellite (x = 1) to chalcocite (x = 2), with energy band gaps between 1.3 and 2.4 eV [19]. The special properties of covellite CuS depend on the specific structure to create a distinct anisotropic metallic conductivity and an inherent high degree of hole delocalization [20]. Control over the shape, size, and nanostructure surface chemistry adjustments play a vital role in their choice of applications [21]. Mn-doped QDs have been used in QDSSCs through the commonly used successive ionic layer absorption and reaction technique to coat Mn ions on the semiconductor QD surface [22, 23]. Wang et al. used the inert reaction system in the single-source precursor (SSP) approach [17, 24, 25]. In this study, MnS and CuS QDs were prepared through SSPs, and the co-sensitization deposition for each material was done with TiO$_2$ to alter the inherent QD properties, thereby increasing the light-harvesting potential of the assembled cells. In addition, the passivation of MnS with CuS exhibits a positive effect of charge transfer collection and light harvesting on the cell performance of QDSSCs under simulated illumination of 100 mWcm$^2$.

## 2 Results

### 2.1 XRD, Raman and FTIR analysis

The X-ray diffraction patterns of CM-1, CM-2, and CM-3 prepared devices are given in Fig. 1a, consisting of minor-phase CuS and MnS as major phases, with sharp peaks demonstrating their good crystallinity. The diffraction characteristic peaks are indexed to the planes (100), (002), (006) and (012), which agree with the hexagonal MnS crystallites (JCPD file No. 96-153-8837). The diffraction peaks around 2θ = 31.81º and 51.66º characteristic to the indexed plane of (013) and (999) for the orthorhombic CuS crystallites (JCPD file No. 96-900-8391). The phase index (%) was obtained as 22.2: CuS, 77.8: MnS for CM-1, 85.9: CuS, 14.1 MnS for CM-2, and 28.5: CuS, 71.5: MnS for CM-3. While the elements (%) for Cu, S, and Mn are 14.7, 36.1, and 49.1 for CM-1, 57.1, 34, and 8.9 for CM-2, and 18.9, 35.9, and 45.1 for CM-3 using crystal impact software. An increase in the carbon composition coming from the molecules used in the formation of CuS and MnS resulted in an increase in the calculated crystallite size of the as-synthesized devices, as presented in Table 1. The crystallite sizes were obtained using the Scherrer formula for the three samples [26].

$$D = \frac{k\lambda}{\beta cos\theta} \tag{1}$$

where D is the crystal size, $k$ is a constant typically 0.9, $\lambda$ = 0.15406 nm is the wavelength of the X-ray, $\beta$ is the full-width half maximum of the diffraction peaks (FWHM) and θ is the diffraction angle. We could also link the increase to the variation in the ionic radii of Mn and Cu cations, which led to a slight shift in the diffraction peaks positions in the crystalline phases. This study reveals that the good crystallization is linked to the nature of the amine used for the formation of metal sulfides, which is supported by the TEM results [27]. Figure 1b, reveals the FTIR spectra of CM-1, CM-2, and CM-3 heterostructure solar cell devices within the range of 4000–500 cm$^{-1}$. The band from 539 to 580 cm$^{-1}$ (M-S) corresponds to the bonds for Mn-S and Cu–S stretching of MnS and CuS phases. The small absorption bands found around 407–427 cm$^{-1}$ are ascribed to the vibrational modes of sulfide ion resonance interactions, while the C–S vibrations stretching are detected around 717–720 cm$^{-1}$. The scissoring vibration absorption between 1633–1468 cm$^{-1}$ and 3313 cm$^{-1}$ is linked to the C–N and the N–H stretching [28]. The asymmetric vibration band at 2930–2918 cm$^{-1}$ represents the vibrational modes of CH$_2$ and C–H stretching [29]. Atomic vibrational modes illustrating the spatial variations and surface species of a thin film are identified from Raman measurements. The as-prepared modified electrodes with typical Raman spectra are presented in Fig. 1c. Three Raman peaks were detected at 269, 398, and 610 cm$^{-1}$ for CM-1, 251, 397, and 612 cm$^{-1}$ for CM-2, and 260, 415, and 508 cm$^{-1}$ for CM-3. The first weak peaks are indexed to the Cu–S stretching vibration, while the second and third

**Fig. 1** X-ray diffraction patterns (**a**), FTIR spectra (**b**) and Raman spectra (**c**) of CM-1, CM-2 and CM-3 devices
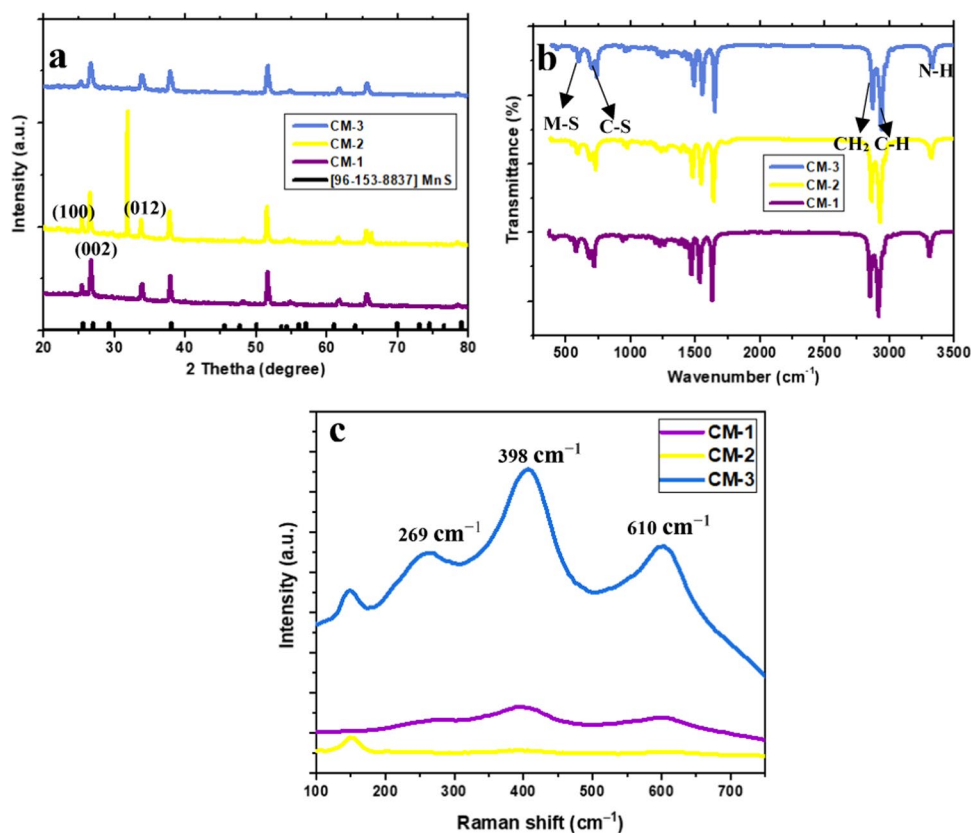


peaks are linked to the Mn-S bond vibrations in MnS. The combination of this heterostructure means that the energy change is triggered by the variation in particle size and surface effect, thus resulting in good electronic conductivity. These results are in good agreement with the FTIR observation and previous reported results [30, 31].

## 2.2  UV–Vis and band gap analysis

Figure 2a and the inserted Fig. b show the UV–visible absorption spectra of CM-1, CM-2, and CM-3 modified cells. The broad adsorption bands at 300 nm are linked to the π-π transition of the phenyl rings of the molecular precursors, which are consistent with the results from the FTIR studies [32]. The adsorption capacity could be linked to the structural modification by passivation of CuS with $TiO_2$ and good interaction with MnS. In order to establish the photochemical response of these modified devices, UV–Vis data were circulated through a tauc plot (see Fig. 2b) to obtain the band gap values for the three samples.

$$E_g = \frac{1240}{\lambda}e \qquad (2)$$

The increase in adsorption intensity of CM-1 is ascribed to the visible light activity of $TiO_2$/CuS/MnS [33]. The band gap energy for CM-1 at 3.49 eV is high in comparison to those of CM-2 and CM-3 cells at 2.70 eV and 2.90 eV, respectively. These narrow band gaps could be attributed to good interaction between the passivative material on the $TiO_2$ surface or to the wrapping of the components of the system [32, 33].

## 2.3  EIS and Bode plot analysis

EIS was used to evaluate the internal electron transfer kinetics of the three assembled devices consisting of CM-1, CM-2, and CM-3, which were measured and displayed in Fig. 3a–c. The model adopted for the extraction of impedance and the capacitive value are obtained using Eqs. (3–6), which is similar to the literature by [34, 35].

The inset equivalent circuits on each Nyquist plot can be used to fit the curves shown in Fig. 3a–c. The effective impedance of CM-3 can be estimated using Eq. (4) while that of CM-1 and CM-2 is best approximated using (3–5).

**Table 1** XRD parameters of CuS and MnS for CM-1, CM-2 and CM-3 devices

| No | 2theta [º] | d [Å] | Miller indices [hkl] | FWHM | Size distribution [nm] |
|---|---|---|---|---|---|
| | | | CM-1 | | |
| 1 | 25.41 | 3.5025 | H (100) | 0.3150 | 27.01 |
| 2 | 25.93 | 3.4328 | | 0.3150 | 27.04 |
| 3 | 26.70 | 3.3366 | H (002) | 0.2625 | 32.50 |
| 4 | 33.86 | 2.6451 | H (006) | 0.3150 | 27.55 |
| 5 | 37.88 | 2.3733 | H (012) | 0.3150 | 27.86 |
| 6 | 51.63 | 1.7688 | O (999) | 0.2625 | 35.13 |
| 7 | 61.69 | 1.5025 | | 0.4200 | 23.02 |
| 8 | 65.62 | 1.4215 | | 0.4200 | 23.52 |
| | | | | | Average 27.95 |
| | | | CM-2 | | |
| 1 | 22.00 | 4.0376 | | 0.4200 | 20.13 |
| 2 | 22.71 | 3.9131 | | 0.8925 | 9.49 |
| 3 | 25.23 | 3.5276 | H (100) | 0.4725 | 18.00 |
| 4 | 26.67 | 3.3398 | H (002) | 0.4200 | 20.31 |
| 5 | 33.86 | 2.6451 | H (006) | 0.4725 | 18.36 |
| 6 | 37.88 | 2.3733 | | 0.4200 | 18.67 |
| 7 | 51.66 | 1.7680 | O (999) | 0.4725 | 19.52 |
| 8 | 61.66 | 1.5030 | | 0.4725 | 20.46 |
| 9 | 65.62 | 1.4215 | | 0.4200 | 23.52 |
| | | | | | Average 18.71 |
| | | | CM-3 | | |
| 1 | 25.41 | 3.5025 | H (100) | 0.2625 | 32.42 |
| 2 | 26.56 | 3.3528 | H (002) | 0.2625 | 32.49 |
| 3 | 31.79 | 2.8128 | | 0.1050 | 82.20 |
| 4 | 31.81 | 2.8105 | | 0.1050 | 82.20 |
| 5 | 33.76 | 2.6531 | H (006) | 0.2625 | 33.05 |
| 6 | 37.77 | 2.3797 | H (012) | 0.2625 | 33.42 |
| 7 | 51.53 | 1.7722 | O (999) | 0.2100 | 43.89 |
| 8 | 65.49 | 1.4240 | | 0.2625 | 37.60 |
| | | | | | Average 47.15 |
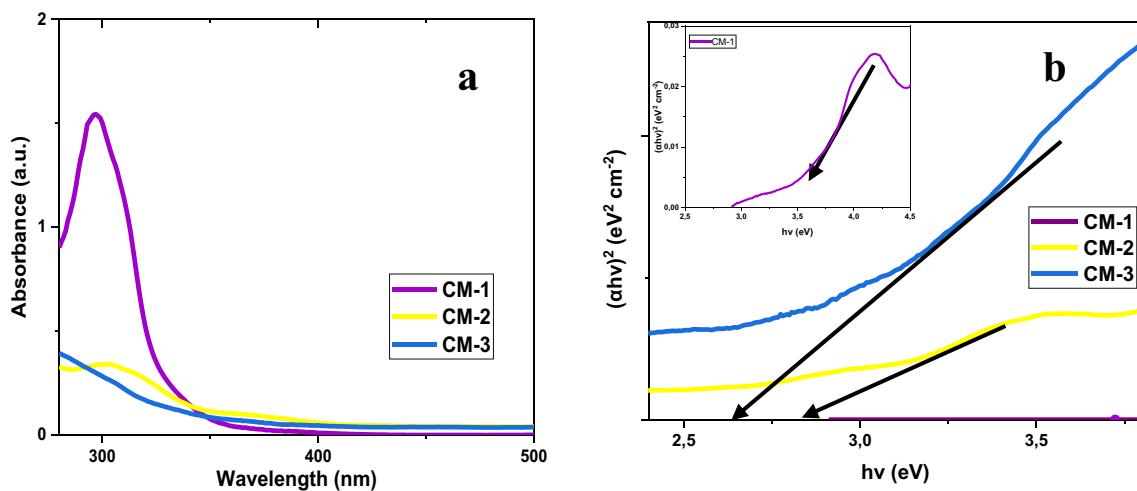


**Fig. 2** UV–Vis spectrum (**a**) and Tauc plot (**b**) of CM-1, CM-2 and CM-3 devices
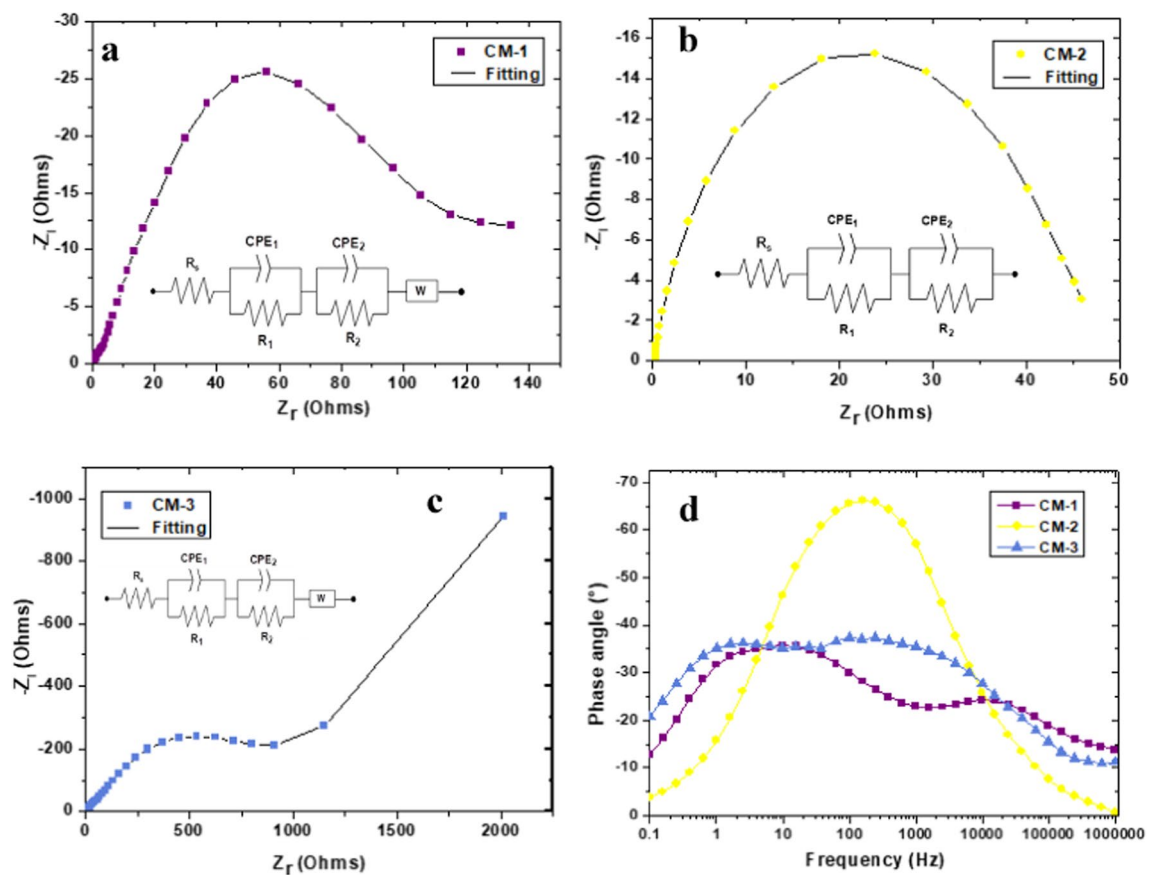
**Fig. 3** EIS Nyquist plots (**a**–**c**) and Bode plot (**d**) of CM-1, CM-2 and CM-3 devices

$$Z_{total} = R_s + \frac{R_1}{1 + R_1\left(Z_{CPE1}\right)^{-1}} \frac{R_2}{1 + R_2\left(Z_{CPE2}\right)^{-1}} \tag{3}$$

$$Z_T = R_s + Z_1 \tag{4}$$

$$Z_1 = \left(\frac{1}{R_s + Z_W} + \frac{1}{Z_{CPE}}\right)^{-1} \tag{5}$$

where, $R_s$ is the electrode/wafer series resistance measured as real-axis shift from the origin of the impedance (Nyquist) curve, and $Z_{CPE}$ estimates the impure capacitive effect across the bulk of the cell-type while $Z_w$ is referred to as Warburg impedance. $Z_w$ describes a much slower charge carrier diffusion and is observed as an arc starting at an approximate angle of $45^0$. It can be estimated using (6), where σ is the Warburg coefficient.

$$Z_w = \frac{\sigma}{\sqrt{2\pi f}} - j\frac{\sigma}{\sqrt{2\pi f}} \tag{6}$$

where σ is the Warburg coefficient defined as

$$\sigma = \frac{RT}{n^2 F^2 \sqrt{2}}\left(\frac{1}{C_O(D_O)^{1/2}} + \frac{1}{C_R(D_R)^{1/2}}\right) \tag{7}$$

From (7), D represents diffusion coefficient, R, T and F are the ideal gas constant, absolute temperature, and Faraday constant respectively. Subscripts "$_O$" and "$_R$" represent the oxidation and reduction species. "$C$" and "$D$" are the concentration and diffusivities of the species while "$n$" is the number of electrons transferred.

The values of the intrinsic resistance parameters for each of CM-1, CM-2 and CM3 obtained from the EIS data and fitted with a transmission line model using Gamry software are as follows: $R_s$ = 1.552 (±0.0483) Ω, 1.576 (±0.0286) Ω, 2.460 (±0.0480) Ω; $R_1$ = 18.936 (±0.5062) Ω, 46.602 (±0.5203), 27.109 (±0.8233) Ω; $R_2$ = 127.7481 (±3.852) Ω, 2.194 (±0.7972) Ω, 180.9105 (±7.857) Ω respectively. While the warburg coefficient for CM-1 and CM-3 are 0.0011 Ω s$^{1/2}$ and 0.0028 Ω s$^{1/2}$ respectively. From Fig. 3a–c, the overall measured impedance of CM-2 was significantly smaller than that of CM-1 and CM-3 under same testing conditions. These results indicate that the CM-2 device offers lower overall resistance to mobile charge carriers and therefore more effective in improving electron charge transfer rate. This increased electrolytic ion transport, which could be attributed to the TiO$_2$/CuS/MnS electrode's homogenous surface, provides more effective active area for the iodolyte HI-30 electrolyte and facilitates their interaction. However, as indicated by the Bode plot in Fig. 3d, CM-2 has higher charge trasnfer rate compared to CM-3 which shows a Warburg impedance effect representing slower ion diffusion mechanism across the iodolyte HI-30 electrolyte. This implies that the CM-2 passivation of the CuS layer enhances the charge transport process and suppresses charge recombination. This is supported by the increase in $J_{sc}$ and FF, as seen in the J-V parameter in Table 2. The Bode plot for the CM-2 device (see Fig. 3d) shows significant capacitive effect and therefore high charge accumulation at the TiO$_2$/CuS/MnS/electrolyte interface. This feature is consistent with findings by Choi et al. [36].

## 2.4 LSV, CV curve and CA analysis

To further examine the role of size distribution, shapes, and optical properties of the three samples, the cell performances of CM-1, CM-2, and CM-3 were evaluated using linear sweep voltammetry (LSV). As displayed in Fig. 4a, the LSV curves reveal excellent cell performance for CM-3, which exhibits a lower over-potential compared to CM-1 and CM-2 [37]. The CV curves of the CM-1, CM-2, and CM-3 solar cell devices (active film area 0.25 cm$^2$) at a scan rate of 100 mV/s, as shown in Fig. 4b, were used for the evaluation of the catalytic activity of the three devices. Figure 4b shows that CM-1 devices have a higher current density than CM-2, suggesting that CM-1 not only promotes the rapid electron transport and diffusion rate of redox conjugates but also has consistent catalytic activity for the reduction of polysulfide electrolytes. The CM-3 device has the highest current density due to its better electrocatalytic activity, indicating that the assembled solar cell device of the CM-3 has better performance. [38, 39]. Chronoamperometry analysis was employed to study the stability of the devices in Fig. 4c, using the Cottrell Eq. (8) showing the total current as a function of time.

$$i(t) = \frac{nFAD_0^{1/2}C_0^*}{\pi^{1/2}t^{1/2}} \tag{8}$$

where i(t) is current, n is the number of electrons transferred in the half reaction, F is Faraday's Constant, A is the area of the electrode, $D_0$ is the diffusion coefficient, $C_o^*$ is the initial concentration, and t is time. For the CM-2 sample, the total current slightly decreased with time at the initial state due to the ionic species depletion in the electrolyte, which implies that the cell is polarized and current flows due to the electron migration across the electrolyte and interfaces at this steady state. The CM-1 and CM-3 exhibited a fully depleted situation.

## 2.5 I–V curve analysis

In this study, the J – V curves of the QDSCs devices were further analysed as illustrated in Fig. 4d. The QDSCs photoelectric properties, such as the short-circuit current density (Jsc), open circuit voltage (Voc), fill factor (FF), and conversion efficiency (η), are listed in Table 2. The values shown in Table 2 are the averaged values and standard

| Table 2 I–V parameters for CM-1, CM-2 and CM-3 devices | Samples | $V_{OC}$ (V) | $J_{SC}$ (mA/cm$^2$) | FF | η (%) | $P_{max}$ (W) |
|---|---|---|---|---|---|---|
| | CM-1 | 0.59±0.01 | 11±0.01 | 0.80±0.01 | 5.20±0.01 | 5.22 |
| | CM-2 | 0.59±0.01 | 14±0.0 | 0.83±0.02 | 6.85±0.02 | 6.86 |
| | CM-3 | 0.65±0.01 | 10.8±0.02 | 0.81±0.01 | 5.68±0.01 | 5.70 |
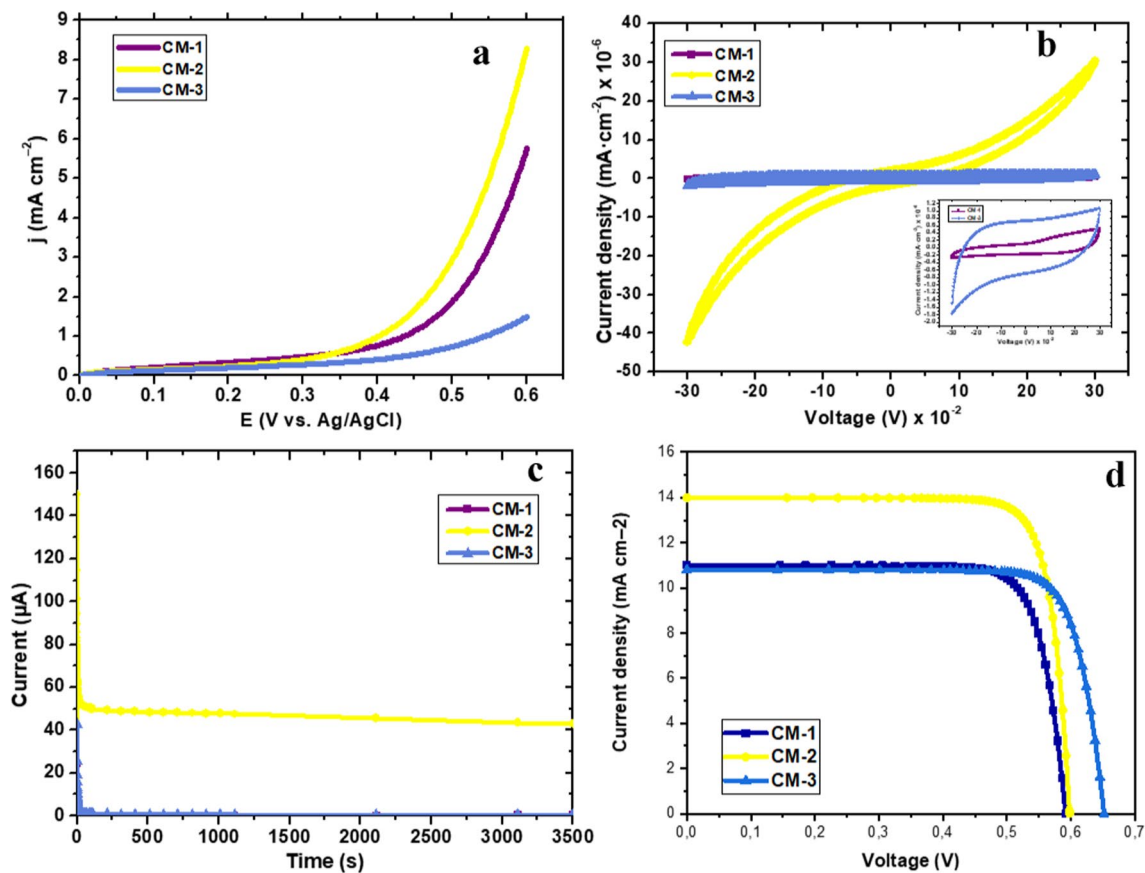
**Fig. 4** LSV curves (**a**), CV curve (**b**), Chronoamperometry analysis (**c**) and I-V curve (**d**) of CM-1, CM-2 and CM-3 devices

deviations of the three devices made under identical conditions and compared with literature on passiavtive cells as shown in Table 3. The $Jsc$ of the CM-1 was 11 mA/cm$^2$, 14 mA/cm$^2$ for the CM-2, and 10.8 mA/cm$^2$ for the CM-3, respectively. However, the $Voc$ was consistent at 0.59 V for CM-1 and CM-2, while the CM-3 was 0.65 V. The $FF$ of the three samples were 0.80, 0.83, and 0.81, respectively; an increase in the particle size and chemical constituents of MnS and CuS led to a rise in the $FF$. The $\eta$ were 5.20%, 6.85%, and 5.68%, respectively. According to the $J–V$ curve analysis, the CM-3 device suggests that the electrons in the conduction band of TiO$_2$ recombine with the semiconductor QDs

| Table 3 Passivation of DSSCs devices | Samples | $V_{OC}$ (V) | $J_{SC}$ (mA/cm$^2$) | FF | η (%) | Ref |
|---|---|---|---|---|---|---|
| | 10% Mn-d-bS/CdS/CdSe/ZnS | 0.53 | 17.34 | 0.48 | 4.25 | [45] |
| | ZnO/ZnS-MnS(0.100)/CdS | 0.55 | 16.60 | 0.40 | 3.62 | [46] |
| | CdSe/CdS/PbS/ZnO | 0.62 | 12.22 | 0.31 | 2.35 | [47] |
| | TiO$_2$/L-CdS/S-CdS | 0.54 | 9.14 | 0.33 | 1.60 | [48] |
| | ZnO/CdS/CdSe/MnS (1 min) | 0.60 | 13.74 | 0.44 | 3.70 | [49] |
| | Mn:QD/Mn:ZnS | 0.685 | 20.83 | 64.7 | 9.23 | [24] |
| | CdSe with ZnS coating | 0.53 | 12.2 | 0.31 | 2.02 | [50] |
| | MnS/CdS/CdSe/ZnS | 0.61 | 13.82 | 0.41 | 3.45 | [17] |
| | CdS/Mn:CdSe | 0.57 | 12.65 | 0.58 | 4.9 | [51] |
| | CdMnSe | 0.58 | 19.15 | 0.57 | 6.33 | [52] |
| | WPF-ZnO-np | 0.55 | 24.81 | 1 0.66 | 9.01 | [53] |
| | PbS-TBAI/PbS-EDT | 0.5546 | 24.2 | 63.8 | 8.55 | [54] |
| | ZnO HMS/TiO$_2$/TiCl$_4$/10-min | 0.45 | 14.57 | 0.46 | 2.99 | [55] |
| | Tri-EAHI | 0.633 | 25.58 | 0.621 | 10.1 | [56] |

and the HI-30 electrolyte. The CM-1 and CM-2 shows that there is a potential barrier that hides the recombination of the electrons at the conduction band of $TiO_2$ with the metal sulfide and the HI-30 electrolyte. This also enabled the electrons to move to the external circuit, thus improving the $\eta$ and $Jsc$ for CM-1 and CM-2 [40]. Also, we can correlate the phase index and the element weight percentage of Cu and S passivation to the enhanced Voc in CM-3.

## 2.6 HRTEM analysis

HRTEM analysis was used to investigate the CuS and MnS nanostructures prepared from different precursors, as illustrated in Fig. 5a–l. TEM images reveal a blend of spherical grains with some agglomerates, which resulted in morphology modifications of the coated electrodes. This indicates clustered nanoparticles of 16.60–60.02 nm were obtained for CM-1 and CM-2, while for CM-3 around 18.26–59.70 nm, as shown in Fig. 5a, e, i. XRD results confirm the same trend as TEM analyses on the size distributions. The inset images in Fig. 5c, g, and k for selected area electron diffraction (SAED) patterns show the crystalline characteristics based on the spots in the ring patterns, grain size, and coalescence of CuS and MnS. The $d$-spacing and line intensity profiles of the corresponding planes (as seen in Fig. 5b, f, j and the inserted Fig. 5d, h, l) of 0.34 nm (002) for MnS, 0.21 nm (006) for CuS and 0.32 nm (002) for MnS for CM-1, CM-2 and CM-3 indicate the significant effect of passivation on morphology, which in turn influences the electrical performance [41].

## 2.7 SEM and EDS analysis

The SEM images of the CM-1, CM-2, and CM-3 prepared devices are provided, as shown in Fig. 6a, c, e, exhibiting a spherical morphology with a closely packed structure. The passivation of the devices shows that CuS can induce the growth of electrodes by forming a porous heterostructure self-assembled device, which promotes more efficient electron transport devices. EDS mapping for the three samples affirmed the presence of C, O, S, Ti, Cu, and Mn elements (as seen in Fig. 6b, d, f), certifying the successful formation of the modified electrode devices [42–44].
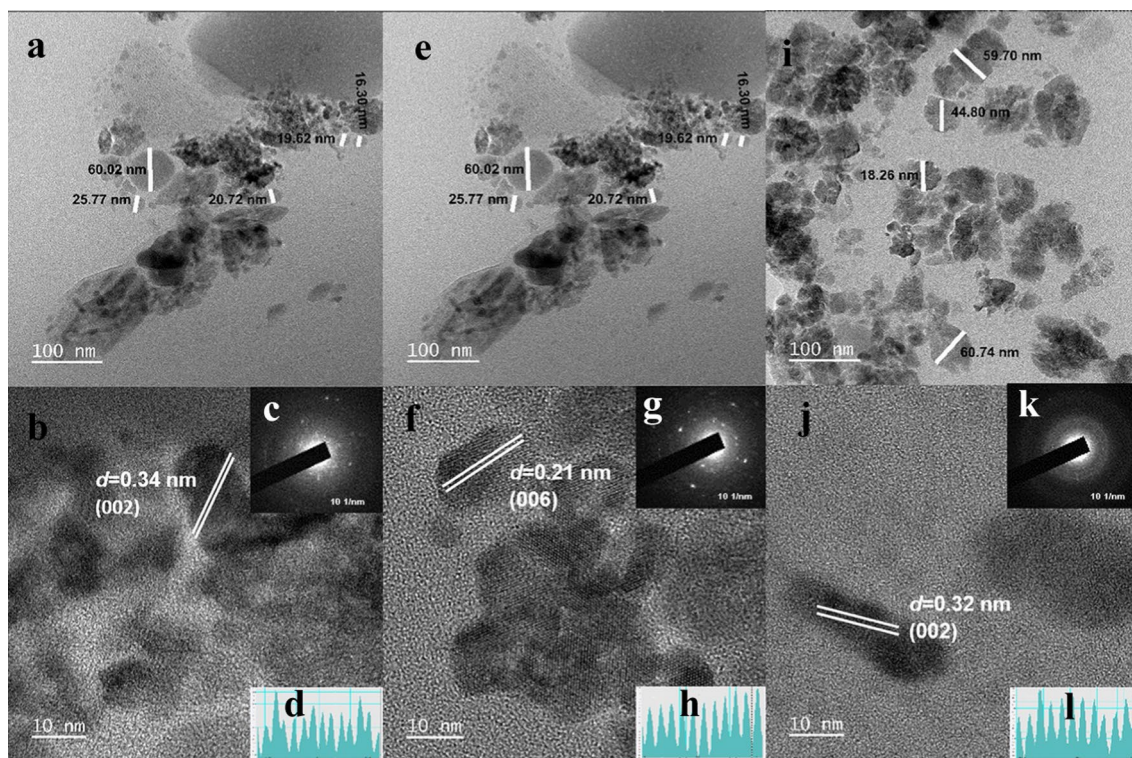


**Fig. 5** TEM, HRTEM and SAED images of CM-1 (**a**–**d**), CM-2 (**e**–**h**) and CM-3 (**i**–**l**) devices

**Fig. 6** SEM and EDS mapping images of CM-1 (**a**, **b**), CM-2 (**c**, **d**) and CM-3 (**e**, **f**) devices
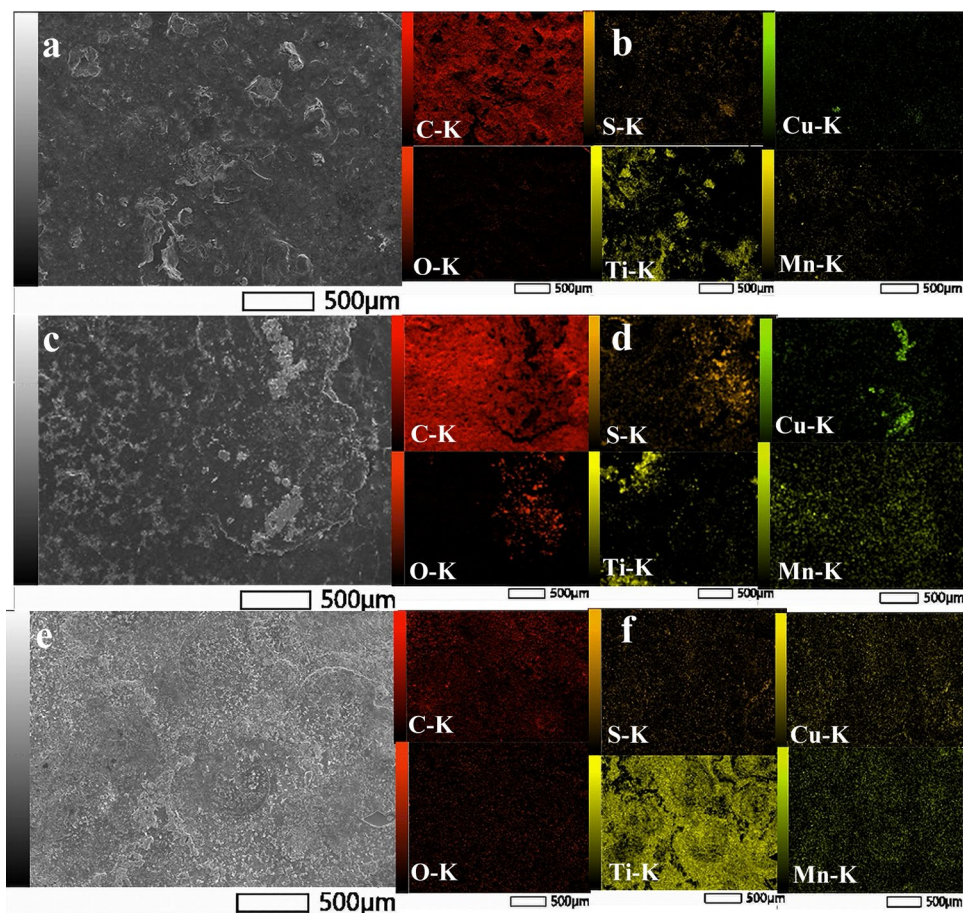


## 3  Conclusions

In summary, heterostructured electrode devices were fabricated using metal sulfides prepared in a one-step solvo-thermal process and applied directly as pasivative and photon absorber nanostructure materials in dye-sensitized solar cells. XRD reveals that the good crystallization of the as-prepared devices is linked to the nature of the amine used for the formation of metal sulfides, as supported by TEM results. The combination of this heterostructure implies that the energy change is triggered by the variation in particle size and surface effect, resulting in good electronic conductivity. The impedance of CM-1 was consistently smaller than that of CM-2, indicating that it is effective in improving the electron transfer rate. The CM-3 device has the highest current density due to its better performance and electrocatalytic activity. The stability of the CM-2 device implies that the cell is polarized and current flows due to electron migration across the electrolyte and interfaces in a steady state. The $\eta$ were 5.20%, 6.85%, and 5.68% for CM-1, CM-2, and CM-3, respectively. These suggest that the electrons in the conduction band of $TiO_2$ recombine with the photon absorbers and the HI-30 electrolyte. Finally, we can conclude that passivation of the as-prepared devices promotes the growth of porous heterostructure self-assembled devices, which promotes more efficient electron transport.

# 4 Experimental

## 4.1 Materials and methods

Complete testing kits containing platinum FTO, fluorine-doped tin oxide (FTO) of TiO$_2$, HI-30 electrolyte iodide, gaskets, masks and hot seal were purchased from Solaronix. Water, CuS and MnS nanoparticles from Cu(II) and Mn(II) complexes of aniline, anisinidine and piperidine aromatic amines.

## 4.2 Synthesis of quantum dots metals sulphides of CuS and MnS

CuS QD nanomaterials were fabricated from the molecular precursors (anil-piper-Cu(DTC)1), (anil-Cu(DTC)2), and (piper-Cu(DTC)3) (a-c) using the SSP approach, as previously reported, to form CuSa, CuSb, and CuSc [3]. While MnS QD were prepared using (a-c) *bis*(*N*-Piperl-*N*-*p*-anisildithiocarbamato)Manganese(II) Complexes, Mn[*N*-Piper-*N*-*p*-Anisdtc] (MnS_1), *N*-*p*-anisidinyldithiocarbamato with MnCl$_2$·4H$_2$O at ratio of 2:1 formulated as Mn[*N*-*p*-anisdtc] (MnS_2) and *N*-piperidinyldithiocarbamato with MnCl$_2$·4H$_2$O at ratio of 2:1 formulated as Mn[*N*-piperdtc] (MnS_3) from our previous study as shown in Fig. 7 [25].
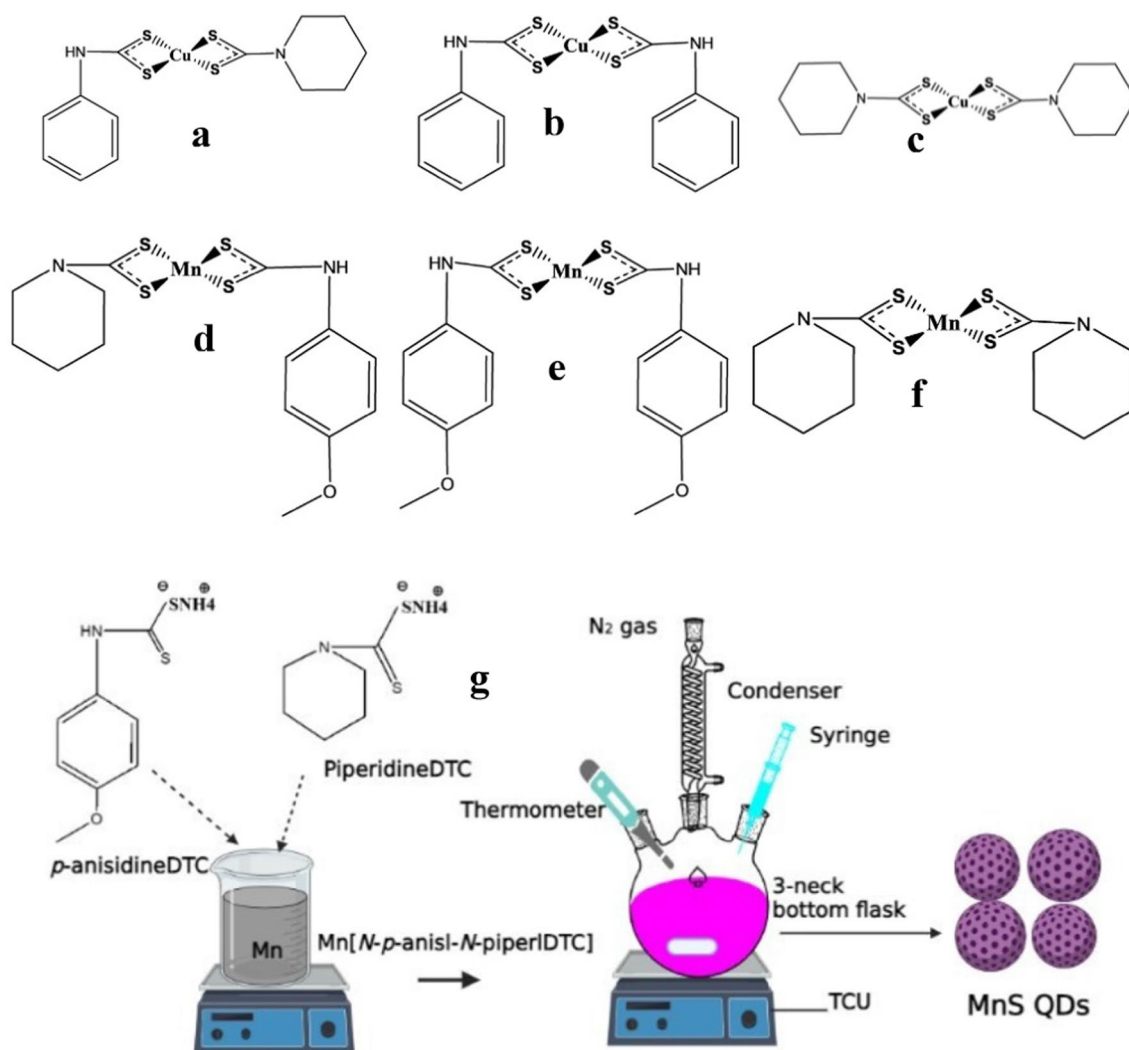


**Fig. 7** Dithiocarbamate complexes (**a–f**) and SSPs approach (**g**) for the synthesis of CuS and MnS

### 4.3  Assembly of DSSCS

The $TiO_2$ film was first immersed in 0.1 g of CuS mixed with distilled water for 10 h, then washed with distilled water and air-dried. Subsequently, the films were immersed in a 0.1 g MnS solution in distilled water for 10 h to allow loading of both materials on the $TiO_2$ [7]. The following materials were combined: CuSa and MnS_1 as CM-1, CuSb and MnS_2 as CM-2, and CuSc and MnS_3 as CM-3. The corresponding films were denoted as CM-1, CM-2, and CM-3. The $TiO_2$ photoanode with MnS and CuS-coated materials and platinum FTO electrodes were clamped and injected with a HI-30 electrolyte, then sealed with hot melt. The effective active surface area of the cell was 0.25 cm$^2$. The overall conversion efficiency were obtained through the following Eq. (9):

$$\eta(\%) = \frac{V_{OC} X I_{SC} X FF}{P_i} \times 100\%$$

(9)

where $V_{OC}$, $I_{SC}$, $FF$, and $P_i$ are the open-circuit voltage, short-circuit current, fill factor and input power ($mWcm^{-2}$) respectively.

### 4.4  Physical characterizations

X-ray diffraction was taken within a rotation anode high-power X-ray diffractometer (Bruker D8 Advance) with Cu-Ka radiation (k = 1.5406 A °) at 40 kV and 40 mA. Surface morphology and the chemical constituents of the fabricated DSSC cells were analyzed via field emission scanning electron microscopy and X-ray energy-dispersive spectroscopy using FESEM, JEOL, JSM-6700F, 5 kV with a Nanotrace EDX detector (Thermo Electron) and transmission electron microscopy (TEM, JEOL JEM-2010) at 200 kV. Functional group identification was taken from the Fourier transform infrared FTIR using the Perkin Elmer Spectrum 1. The optical properties of the cells were measured using a UV–visible spectrometer by Perkin Elmer-Lamda 45. Keithley 2400 with Source Meter (AM) 1.5G (1000 Wm$^{-2}$) was used to measure the J-V properties of the as-prepared devices. A Gamry 10101E electrochemical workstation equipped with a three-electrode device was employed to evaluate the electrocatalytic performance of the three samples. The electrochemical impedance spectra (EIS) were analyzed operating at a frequency range of 1 kHz–10$^7$ Hz at 10 mV. Cyclic voltammetry (CV) and linear sweep voltammetry (LSV) analysis were measured at scan rates of 100 and 10 mV s$^{-1}$. Chronoamperometry (CA) was evaluated to study the effect of passivation on the stability of the cells.

**Data availability**  The data supporting the results of this investigation are included in the manuscript.

### Declarations

Discover

# References

1.  Yella A, Lee HW, Tsao HN, Yi C, Chandiran AK, Nazeeruddin MK, Diau EWG, Yeh CY, Zakeeruddin SM, Grätzel M. Porphyrin-sensitized solar cells with cobalt (II/III)–based redox electrolyte exceed 12 percent efficiency. Science. 2011;334:629–34.
2.  Agoro MA, Meyer EL. The formation of SnS nanorods orthorhombic phases grown from different molecular precursors. Results Chem. 2023;5: 100690.
3.  Agoro MA, Meyer EL. Influence of a one-pot approach on a prepared CuS macro/nanostructure from various molecular precursors. Inorganics. 2023;11:266.
4.  Mathew S, Yella A, Gao P, Humphry-Baker R, Curchod BF, Ashari-Astani N, Tavernelli I, Rothlisberger U, Nazeeruddin MK, Grätzel M. Dye-sensitized solar cells with 13% efficiency achieved through the molecular engineering of porphyrin sensitizers. Nat Chem. 2014;6:242–7.
5.  Higashino T, Imahori H. Porphyrins as excellent dyes for dye-sensitized solar cells: recent developments and insights. Dalton Trans. 2015;44:448–63.
6.  Yen YC, Lin CC, Chen PY, Ko WY, Tien TR, Lin KJ. Green synthesis of carbon quantum dots embedded onto titanium dioxide nanowires for enhancing photocurrent. R Soc Open Sci. 2017;4: 161051.
7.  Agoro MA, Meyer EL, Mbese JZ, Fuku X, Ahia CC. Aliphatic mixed ligands Sn(II) complexes as photon absorbers in quantum dots sensitized solar cell. J Solid State Chem. 2022;308: 122890.
8.  Shen X, Jia J, Lin Y, Zhou X. Enhanced performance of CdTe quantum dot sensitized solar cell via anion exchanges. J Power Sources. 2015;277:215–21.
9.  Jumabekov AN, Siegler TD, Cordes N, Medina DD, Böhm D, Garbus P, Meroni S, Peter LM, Bein T. Comparison of solid-state quantum-dot-sensitized solar cells with ex situ and in situ grown PbS quantum dots. J Phys Chem C. 2014;118:25853–62.
10. Jara DH, Yoon SJ, Stamplecoskie KG, Kamat PV. Size-dependent photovoltaic performance of CuInS$_2$ quantum dot-sensitized solar cells. Chem Mater. 2014;26:7221–8.
11. Li W, Pan Z, Zhong X. CuInSe$_2$ and CuInSe$_2$–ZnS based high efficiency "green" quantum dot sensitized solar cells. J Mater Chem A. 2015;3:1649–55.
12. Lee YL, Lo YS. Highly efficient quantum-dot-sensitized solar cell based on co-sensitization of CdS/CdSe. Adv Funct Mater. 2009;19:604–9.
13. Santra PK, Kamat PV. Mn-doped quantum dot sensitized solar cells: a strategy to boost efficiency over 5%. JACS. 2012;134:2508–11.
14. Zhong Y, Zhang H, Pan D, Wang L, Zhong X. Graphene quantum dots assisted photovoltage and efficiency enhancement in CdSe quantum dot sensitized solar cells. Energy Chem. 2015;24:722–8.
15. Sahasrabudhe A, Bhattacharyya S. Dual sensitization strategy for high-performance core/shell/quasi-shell quantum dot solar cells. Chem Mater. 2015;27:4848–59.
16. Zhao K, Pan Z, Mora-Seró I, Cánovas E, Wang H, Song Y, Gong X, Wang J, Bonn M, Bisquert J, Zhong X. Boosting power conversion efficiencies of quantum-dot-sensitized solar cells beyond 8% by recombination control. JACS. 2015;137:5602–9.
17. Zhang C, Liu S, Liu X, Deng F, Xiong Y, Tsai FC. Incorporation of Mn$^{2+}$ into CdSe quantum dots by chemical bath co-deposition method for photovoltaic enhancement of quantum dot-sensitized solar cells. R Soc Open Sci. 2018;5:171712.
18. Taha AA, Al-Jawad SM, Salim MM. Influence of titanium tetraisopropoxide concentration on the antibacterial activity of TiO$_2$ thin films. Surf Rev Lett. 2018;25:1850111.
19. Al-Jawad SM, Taha AA, Muhsen MM. Preparation and characterization of CuS nanoparticles prepared by two-phase colloidal method. JPCS. 2021;1795:012053.
20. Kumar P, Nagarajan R, Sarangi R. Quantitative X-ray absorption and emission spectroscopies: electronic structure elucidation of Cu$_2$S and CuS. J Mater Chem C. 2013;1:2448–54.
21. Lesyuk R, Klein E, Yaremchuk I, Klinke C. Copper sulfide nanosheets with shape-tunable plasmonic properties in the NIR region. Nanoscale. 2018;10:20640–51.
22. Venkata-Haritha M, Gopi CV, Thulasi-Varma CV, Kim SK, Kim HJ. Influence of Mn$^{+2}$ incorporation in CdSe quantum dots for high performance of CdS–CdSe quantum dot sensitized solar cells. J Photochem Photobiol A Chem. 2016;315:34–41.
23. Kim SK, Gopi CV, Lee JC, Kim HJ. Enhanced performance of branched TiO$_2$ nanorod based Mn-doped CdS and Mn-doped CdSe quantum dot-sensitized solar cell. J Appl Phys. 2015. https://doi.org/10.1063/1.4918913.
24. Wang J, Li Y, Shen Q, Izuishi T, Pan Z, Zhao K, Zhong X. Mn doped quantum dot sensitized solar cells with power conversion efficiency exceeding 9%. J Mater Chem A. 2016;4:877–86.
25. Agoro MA, Meyer EL. Proficient one-step heat-up synthesis of manganese sulfide quantum dots for solar cell applications. Molecules. 2022;27:6678.
26. Veeramanikandasamy T, Rajendran K, Sambath K, Rameshbabu P. Effect of Cu-doping on optical, electrical and magnetic properties of chemically synthesized MnS nanocrystals. Mater Chem Phys. 2016;171:328–35.
27. Salem SM, Deraz NM, Saleh HA. Fabrication and characterization of chemically deposited copper–manganese sulfide thin films. Appl Phys A. 2020;126:700.
28. Heiba ZK, Mohamed MB, Farag NM, Ahmed SI. Correlation between structural and optical characteristics upon changing the composition ratio of CuS@ MnS nanocomposites. Appl Phys A. 2021;127:1–11.
29. Hu D, Peng H, Peng Y, Guo J. Synthesis and enhanced luminescence properties of CuS@ YF3: Eu core–shell nanoparticles. Appl Phys A. 2020;126:385.
30. Adhikari S, Sarkar D, Madras G. Hierarchical design of CuS architectures for visible light photocatalysis of 4-chlorophenol. ACS Omega. 2017;2:4009–21.
31. Ismail RA, Al-Samarai AME, Muhammed AM. High-performance nanostructured p-Cu$_2$S/n-Si photodetector prepared by chemical bath deposition technique. J Mater Sci Mater Electron. 2019;30:11807–18.
32. Poudel MB, Yu C, Kim HJ. Synthesis of conducting bifunctional polyaniline@ Mn-TiO$_2$ nanocomposites for supercapacitor electrode and visible light driven photocatalysis. Catalysts. 2020;10:546.

33. Zhao Z, Omer AA, Qin Z, Osman S, Xia L, Singh RP. Cu/N-codoped $TiO_2$ prepared by the sol-gel method for phenanthrene removal under visible light irradiation. ESPR. 2020;27:17530–40.
34. Zhu L, Liu R, Wan Z, Cao W, Dong C, Wang Y, Chen C, Chen J, Naveed F, Kuang J, Lei L. Parallel planar heterojunction strategy enables $Sb_2S_3$ solar cells with efficiency exceeding 8%. Angew Chem Int Ed. 2023;135:202312951.
35. Liu R, Shen Z, Wan Z, Zhu L, Chen J, Dong C, Chen W, Cao W, Chen B, Yuan X, Ding B. Nanoarray heterojunction and its efficient solar cells without negative impact of photogenerated electric field. Commun Phys. 2021;4:177.
36. Choi H, Han J, Kang MS, Song K, Ko J. Aqueous electrolytes based dye-sensitized solar cells using I−/I$^{3−}$ redox couple to achieve≥ 4% power conversion efficiency. Bull Korean Chem Soc. 2014;35:1433–9.
37. Bella F, Galliano S, Falco M, Viscardi G, Barolo C, Grätzel M, Gerbaldi C. Unveiling iodine-based electrolytes chemistry in aqueous dye-sensitized solar cells. Chem Sci. 2016;7:4880–90.
38. Ait-karra A, Zakir O, Ait Baha A, Lasri M, Idouhli R, Elyaagoubi M, Abouelfida A, Khadiri M, Benzakour J. Electrodeposition and characterization of copper sulfide (CuS) thin film: towards an understanding of the growth mechanism. J Solid State Electrochem. 2023;27:2051–65.
39. Palve BM, Kadam VS, Jagtap CV, Jadkar SR, Pathan HM. A simple chemical route to synthesis the CuSe and CuS counter electrodes for titanium oxide based quantum dot solar cells. J Mater Sci Mater Electron. 2017;28:14394–401.
40. Liu D, Liu J, Liu J, Liu S, Wang C, Ge Z, Hao X, Du N, Xiao H. The effect of CuS counter electrodes for the CdS/CdSe quantum dot co-sensitized solar cells based on zinc titanium mixed metal oxides. J Mater Sci. 2019;54:4884–92.
41. Orletsky IG, Ilashchuk MI, Maistruk EV, Parkhomenko HP, Marianchuk PD, Koziarskyi IP, Koziarskyi DP. Electrical properties of heterostructures MnS/n-CdZnTe obtained by spray pyrolysis. Mater Res Express. 2021;8: 015905.
42. Sharma KP, Shin M, Awasthi GP, Yu C. Single step hydrothermal synthesis of CuS/MnS composite for electrochemical non-enzymatic glucose sensor. Solid State Sci. 2023;143: 107279.
43. Kannangara YY, Prabunathan P, Song JK. Facile synthesis of a hierarchical CuS/CuSCN nanocomposite with advanced energy storage properties. New J Chem. 2018;42:15387–96.
44. Li W, Song W, Wang H, Kang YM. In situ self-assembly of $Ni_3S_2$/MnS/CuS/reduced graphene composite on nickel foam for high power supercapacitors. RSC Adv. 2019;9:31532–42.
45. Punnoose D, Rao SS, Kim SK, Kim HJ. Exploring the effect of manganese in lead sulfide quantum dot sensitized solar cell to enhance the photovoltaic performance. RSC Adv. 2015;5:33136–45.
46. Shen W, Zhang J, Wang S, Du H, Tang Y. Improve the performance of the quantum dot sensitized ZnO nanotube solar cells with inserting ZnS-MnS composites layers. J Alloys Compd. 2019;787:751–8.
47. Raj CJ, Karthick SN, Park S, Hemalatha KV, Kim SK, Prabakar K, Kim HJ. Improved photovoltaic performance of CdSe/CdS/PbS quantum dot sensitized ZnO nanorod array solar cell. J Power Sources. 2014;248:439–46.
48. Chen H, Li W, Liu H, Zhu L. Performance enhancement of CdS-sensitized $TiO_2$ mesoporous electrode with two different sizes of CdS nanoparticles. Microporous Mesoporous Mater. 2011;138:235–8.
49. Luo J, Wang YX, Sun J, Yang ZS, Zhang QF. MnS passivation layer for highly efficient ZnO–based quantum dot-sensitized solar cells. Sol Energy Mater Sol Cells. 2018;187:199–206.
50. Shen Q, Kobayashi J, Diguna LJ, Toyoda T. Effect of ZnS coating on the photovoltaic properties of CdSe quantum dot-sensitized solar cells. J Appl Phys. 2008. https://doi.org/10.1063/1.2903059.
51. Luo J, Sun J, Guo PC, Yang ZS, Wang YX, Zhang QF. Enhancement in efficiency of CdS/CdSe quantum dots-sensitized solar cells based on ZnO nanostructures by introduction of MnS layer. Mater Lett. 2018;215:176–8.
52. Tian J, Lv L, Fei C, Wang Y, Liu X, Cao G. A highly efficient (> 6%) $Cd_{1−x}$ Mn x Se quantum dot sensitized solar cell. J Mater Chem A. 2014;2:19653–9.
53. Azmi R, Aqoma H, Hadmojo WT, Yun JM, Yoon S, Kim K, Do YR, Oh SH, Jang SY. Low-temperature-processed 9% colloidal quantum dot photovoltaic devices through interfacial management of p–n heterojunction. Adv Energy Mater. 2016;6:1502146.
54. Chuang CHM, Brown PR, Bulović V, Bawendi MG. Improved performance and stability in quantum dot solar cells through band alignment engineering. Nat Mater. 2014;13:796–801.
55. Li Z, Yu L, Wang H, Yang H, Ma H. $TiO_2$ passivation layer on ZnO hollow microspheres for quantum dots sensitized solar cells with improved light harvesting and electron collection. Nanomaterials. 2020;10:631.
56. Park D, Choe G, Kim SC, Yim S. Improved surface passivation of lead sulfide quantum dots using less sterically crowded alkylammonium iodides. Appl Surf Sci. 2023;610: 155431.

Discover